Micro-cavity optimization for ultra-sensitive all-dielectric optical sensors

Paul Rouquette, Claude Amra, Myriam Zerrad, Michel Lequime

Research Article | Vol. 30, No. 9 / 25 Apr 2022 / Optics Express 15344
Optics EXPRESS

Micro-cavity optimization for ultra-sensitive all-dielectric optical sensors

PAUL ROUQUETTE,[1,2,*] CLAUDE AMRA,[1] MYRIAM ZERRAD,[1] AND MICHEL LEQUIME[1]

[1]Aix Marseille Univ., CNRS, Centrale Marseille, Institut Fresnel, Faculté des Sciences - Campus Saint Jérôme, Avenue Escadrille Normandie-Niemen, 13397 Marseille, France
[2]CILAS ArianeGroup, 600 avenue de La Roche Fourcade, Pôle Alpha-Sud, 13400 Aubagne, France
*paul.rouquette@fresnel.fr

Abstract: We present an analytical method for the optimization of luminescent micro-cavities to create a substrate that is extremely sensitive to contamination. Giant optical enhancement can thus be controlled arbitrarily and simultaneously at various frequencies within the substrate's evanescent field with the aim of obtaining ultra-sensitive optical sensors. This process provides an alternative to sensors based on illumination in free space.

1. Introduction

Within the field of optical sensors [1–4], significant progress has been made over the last few years, drawing in particular on studies of the processes of giant enhancement of the electromagnetic field [5–19]. Among the various methods that create these enhancements, all-dielectric planar optical multilayers [20–24] play an essential role because they provide a large number of degrees of freedom for optimizing the design of optical enhancement. In this context we proposed an analytical technique to optimize huge field enhancement in multilayers under arbitrary illumination conditions, relying on the concept of zero-admittance layers [17].

However, we must highlight the fact that these multi-dielectric sensors have, until now, been far-field illuminated via free space (Fig. 1, left diagram), and that the monochromatic detection of contaminants comes about through analysis of the spatial distortion of the reflected beam [19]. Indeed, in contrast to plasmonic systems, there are no absorption peaks for these dielectric components since their overall reflection is always unity. Consequently, we need to be able to perfectly control and stabilize the illumination band-passes (a fraction of a mrd for divergence, and a few pm for the beam line width), an essential condition [12] for obtaining enhancements of several decades (a few thousand). These constraints lead to the complexity, size and cost of the final system.

In order to mitigate these problems, we here propose an alternative that eliminates the free space illumination system, replacing this illumination with an active (luminescent) layer within the stack. Though the component is still theoretically identical, we refer to a micro-cavity [25–46] in the presence of a near field source (Fig. 1, right diagram). From a technological point of view, the active layer (activated electrically) and the whole component must naturally be made using an epitaxial growth technique involving quantum wells and a crystalline substrate, in contrast to the previously mentioned amorphous components made on glass. This active layer then generates a free space emission pattern in the emerging media. The spatial analysis of the reflected beam can then be replaced by a spectral analysis, avoiding the pixel matrix detector and channeling the light away with an optical fiber in free space. Finally, eliminating both the incident beam and the pixel matrix detector leads to a significant reduction in size and an increase in simplicity; these gains are illustrated in Fig. 2, with on the left the sensor previously used [17–19] that was based on free space illumination, and on the right, the micro-cavity sensor discussed in this paper.

#457061 https://doi.org/10.1364/OE.457061
Journal © 2022 Received 24 Feb 2022; revised 31 Mar 2022; accepted 1 Apr 2022; published 20 Apr 2022

Optics EXPRESS

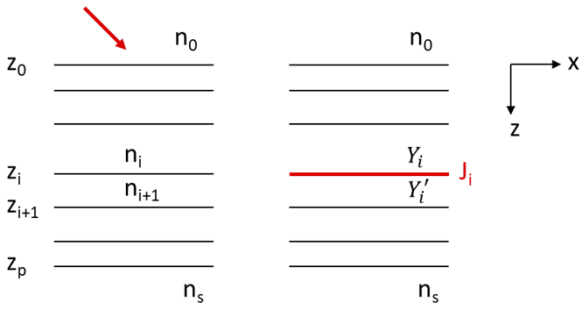

Fig. 1. Optical multilayer illuminated in free space (left figure) or used in the form of a micro-cavity (right figure) with a current at interface i. The two merging media are the substrate (with refractive index n_s) and the superstrate (with refractive index n_0). See text.

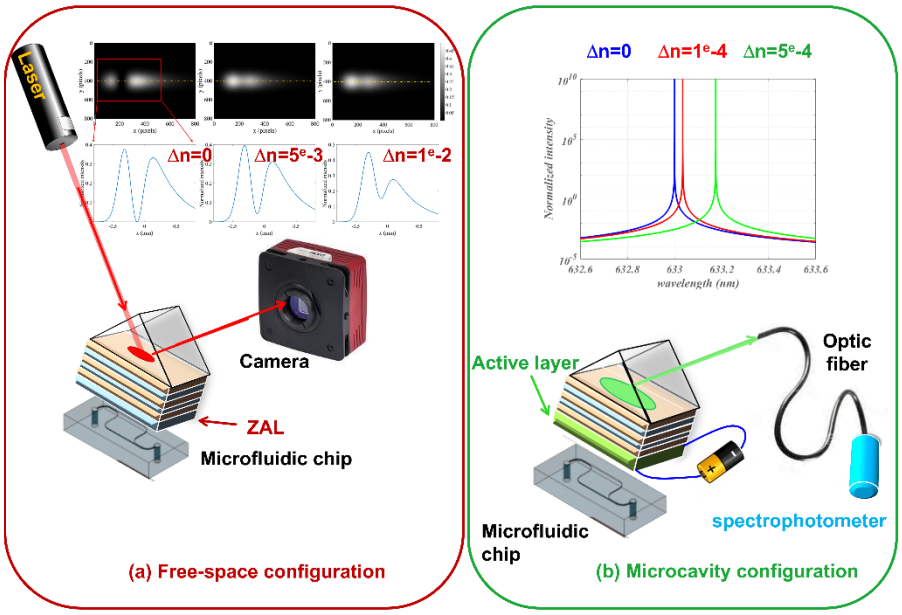

Fig. 2. Free space sensor in a free-space configuration (left), and in the form of a micro-cavity (right). On the right-hand figure note that the prism can be replaced by a decoupling grating.

Optics EXPRESS

For this alternative to be credible, it is important that, for sensor-type applications, the micro-cavity must be capable of re-optimization such that its emission diagram becomes extremely sensitive to any contamination or disturbance of the substrate. This means that we need to synthesize arbitrary giant enhancements within the micro-cavity, as we did [17–19] for free space. Note that the field enhancement must occur in the substrate, so Fabry-Perot type structures are counted out. In this paper our work shows how this optimization can be achieved analytically for arbitrary imposed frequencies, i.e. for different directions of emergence and for different polarizations or wavelengths. These frequencies can also be imposed simultaneously. We show that the levels of performance obtained are similar to those in free space, thus paving the way for a useful alternative, a new type of micro-cavity sensor.

The paper is organized as follows. In section 2 we introduce the formalism and address the general optimization problem in micro-cavities. Solutions lead to classical structures which fit applications in the field of micro-sources but not the field of sensors. In section 3 we consider the micro-cavities under the Total Internal Reflection (TIR) regime. This means that optimization is analytically designed for a specific resonance which gives rise to huge enhancement of the emission pattern in the superstrate, while the field is evanescent in the substrate at this resonance. In section 4 the design technique is extended to multiple resonances, at several wavelengths and angles. The results may find applications both in micro-sources and sensors. All predictions are confirmed by numerical calculation. Eventually we discuss the limits and sensitivity of the cavities in section 5. We show that, although the local quantities (angular fields and emission patterns) may diverge with the layer number of the cavity, the related physical quantities (integrated into the narrow bandwidth of resonance) do not diverge. Conclusion is given in section 6.

2. Micro-cavity optimization in free space with asymptotic poles

We are here interested in optimizing a resonance for free space radiation in emergent media. We use a formalism that we former developed for light scattering in multilayer optics [24,47], and then extended to micro-cavities [24,30,31] and trapped light [24,48]. It is based on macroscopic classical electromagnetism and allows prediction of the emission pattern of sources (electric and magnetic currents) confined within the bulk of multilayer optics. The central tool of this formalism is the complex admittance, a concept that has proven to be very useful for the analytical synthesis of multilayers [20–24]. The key results of this formalism are first recalled.

2.1. Micro-cavity formalism

We consider a monochromatic regime at a single wavelength λ, and the source is described by a surface electric current located at interface (i) of the multilayer. All media are assumed to be linear, homogeneous, isotropic and non-magnetic. The merging media, that is, the superstrate and substrate with refractive indices n_0 and n_s (see Fig. 1), are assumed to be transparent. We work under the assumption of a weak coupling regime, so that there is no interaction between fields and sources.

Under these conditions the power spectral density f_i (per unit of polar angle φ) provided by an electric current J_i at surface (i) within the stack is given as [24,30,31,48]:

$$f_i(\vec{\sigma}) = \frac{\mathrm{dF}}{\mathrm{d}\sigma \mathrm{d}\varphi} = 2\pi^2\sigma\ \Re\left[\frac{1}{\Delta Y_i(\sigma)}\right]\left|\hat{J}_i(\vec{\sigma})\right|^2 \tag{1}$$

where F is the total power provided by the current, and $\hat{J}_i(\vec{\sigma})$ the Fourier transform of $J_i(\vec{r})$, with $\vec{r} = (x, y)$ the transverse spatial variable (see Fig. 1). The conjugate Fourier variable of $\vec{r}$ is the spatial pulsation $\vec{\sigma}$. It is related to the spatial frequency $\vec{\nu}$ by a single coefficient ($\vec{\sigma} = 2\pi\vec{\nu}$), and is also called the angular spatial frequency. This spatial pulsation is the tangential component (see Fig. 3) of the wave vector emitted in the merging media. Hence at low frequencies

Optics EXPRESS

$\sigma = |\vec{\sigma}| < \min(k_0, k_s)$, with $k_i = 2\pi n_i/\lambda$, it can be related to the normal (θ) and polar (φ) emission angles as (Fig. 3):

$$\vec{\sigma} = k_i \sin\theta_i(\cos\varphi, \sin\varphi) \quad \text{with} \quad k_i \sin\theta_i = \text{constant} \tag{2}$$

The quantity $\Delta Y_i = Y_i' - Y_i$ is the difference in the complex admittances from each side of surface (i), that is, in layers (i+1) and (i) respectively (see Fig. 1). Recall that the admittance is the ratio of magnetic to electric field [20,24]. They depend on the observation conditions (wavelength, angle and polarization) and on the multilayer design. They are functions of the z altitude within the stack, and are discontinuous at surface i where the current $\overrightarrow{J_i}(\vec{r})$ is present. In the end media (superstrate and substrate), they identify to the effective indices [20,24].

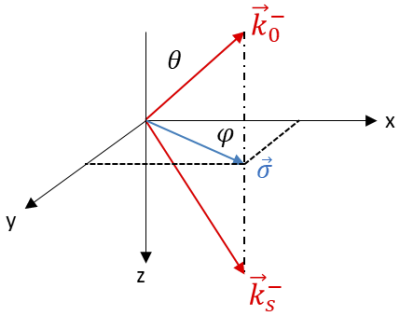

Fig. 3. Normal (θ) and polar (φ) angles of waves in the emergent media, with $\vec{\sigma}$ the spatial pulsation, i.e. the tangential component of the wave vector in the superstrate ($\vec{k}_0^-$) or in the substrate ($\vec{k}_s^+$).

Equation (1) shows how the cavity coefficient $1/\Delta Y_i(\sigma)$ drives the power provided by the current, which can be inhibited or enhanced (at constant current). Note that the power density expressed in Eq. (1) is relative to the total power emitted simultaneously in the merging media (superstrate and substrate), that is, in the half spaces of reflection ($z<z_0$) and transmission ($z>z_p$).

2.2. *Exact (but complex) poles in the modal window*

Equation (1) shows that optimization of the resonances is related to the poles of the cavity factor $\Re\left[\frac{1}{\Delta Y_i(\sigma)}\right]$, and hence to the zeroes of the function $\Delta Y_i(\sigma)$. Therefore, the equation that governs these phenomena is given by:

$$\Delta Y_i(\sigma_m) = \Delta Y(\sigma_m, z = z_i) = 0 \tag{3}$$

where σ_m is the resonance frequency. It is important to note that this condition Eq. (3) is independent of the interface or height z; this is, in fact, a local property that holds throughout the volume of the stack. Indeed, the two admittances Y_i and Y_i' follow the same recurrence relations from one interface to another [20,24]. The difference between these two admittances lies in the initial values of the effective indices $\tilde{n}_i$ they take in the superstrate ($-\tilde{n}_0$ for Y_i) and in the substrate ($\tilde{n}_s$ for Y_i') where the field is no longer stationary, but progressive (propagating in the $z > 0$ direction in the substrate) or retrograde (propagating in the $z < 0$ in the superstrate).

Optics EXPRESS

Therefore, due to similar recurrence relations, the equality of admittances at one height makes them identical at all heights:

$$\Delta Y(\sigma_m, z_i) = 0 \Rightarrow \forall z \;\; \Delta Y(\sigma_m, z) = 0 \tag{4}$$

Furthermore, if we use this property Eq. (4) at the first interface (z_0), we get:

$$\Delta Y_0(\sigma_m) = Y_0' + \tilde{n}_0 = 0 \Rightarrow r_0(\sigma_m) = \frac{\tilde{n}_0 - Y_0'}{\tilde{n}_0 + Y_0'} = \infty \tag{5}$$

where r_0 is the reflection coefficient of the stack [20,24] illuminated on the side of the superstrate whose refractive index is n_0. Hence the solutions σ_m also constitute the poles of the stack's reflection coefficient ($1/r_0(\sigma_m) = 0$), where we know that they are the guided mode propagation constants that, in the absence of any radiative loss, can exist within the structure [24,30,31,48]. Equation (3), Eq. (4) and Eq. (5) are therefore equivalent, which is a key result in mode analysis in multilayers. The solutions to these equations are the modes which mainly depend on the structure of the stack, together with the illumination and observation conditions. Since Eq. (4) is satisfied throughout the stack, it is worth emphasizing the fact that resonances will occur regardless of the position of the source within the component.

The immediate consequence is that, since the solutions to Eq. (5) are those of modes then, in the absence of absorption these solutions σ_m can only exist [24] in the form of real numbers in the modal frequency (or guided wave) window (Fig. 4):

$$\Delta Y_i(\sigma_m) = 0 \Rightarrow \max(k_0, k_s) < \sigma_m < \max(k_i) \tag{6}$$

Conversely, in the free space frequency window (Fig. 4) which is of interest here (we search for the waves travelling in the end media), the solutions to Eq. (5) are necessarily complex, that is:

$$0 < \sigma_m < \max(k_0, k_s) \Rightarrow \Delta Y_i(\sigma_m) \neq 0 \tag{7}$$

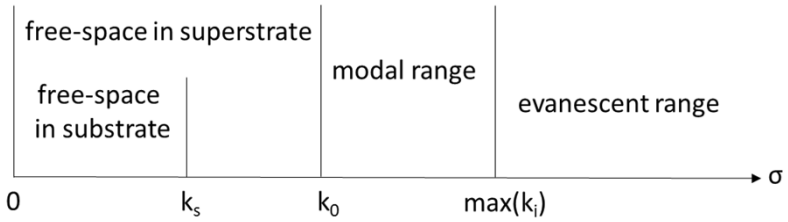

Fig. 4. Free-space and modal frequency windows in terms of spatial pulsation (or angular spatial frequency) σ, for an optical multilayer. The materials' wave numbers are denoted $k_i = 2\pi n_i/\lambda$, with λ the illumination wavelength and n_i the refractive indices of the thin films. k_0 and k_s refer to the superstrate (incident medium) and the substrate respectively. Case $k_s < k_0$.

Hence, in this last free space window we have to be content with adjusting the incident angular frequency σ_m to get the real part of the complex pole, written $\chi_m = \chi_m' + j\chi_m''$, i.e. $\sigma_m \approx \chi_m'$, with:

$$\Delta Y_i(\sigma_m + j\chi_m'') = 0 \tag{8}$$

Such property Eq. (8) is not practical for component design, since it would require identifying and controlling the complex poles with small imaginary parts. Furthermore these complex poles are associated with radiative losses and would reduce the resonance amplitude even for transparent materials. At this step we keep in mind that these exact complex poles cannot be attained in the free-space window, while they are at the origins of huge resonances or field enhancements.

Optics EXPRESS

2.3. Real asymptotic poles in the free-space window

For this reason, another way of proceeding is to approach real poles asymptotically if the number p of layers of the component increases, i.e. in the form:

$$\lim_{p\to\infty} \Delta Y_i(\sigma_m) = 0 \tag{9}$$

In this case the m-order pole χ_m^p of the p-layer structure would tend asymptotically to a real value $\chi'_{m,\infty}$, that is:

$$\lim_{p\to\infty}(\chi_m^p = \chi'_{m,p} + j\chi''_{m,p}) = \chi'_{m,\infty} \Leftrightarrow \lim_{p\to\infty}(\chi''_{m,p}) = 0 \tag{10}$$

Such condition can now be satisfied by the spatial pulsation , and this is the solution that is generally explored indirectly in the literature, leading to Fabry-Perot type structures. Indeed, these structures draw on multi-dielectric mirrors whose energy reflection coefficient $R = |r|^2$ tends to unity with the number of layers p in the structure [20,24], meaning that the admittances tend to 0 ($r = 1$) or to infinity ($r = -1$). Recall the relationship between the top admittance Y_0 and the amplitude reflection coefficient r as:

$$\lim_{p\to\infty}\left\{r(p) = \frac{\tilde{n}_0 - Y_0(p)}{\tilde{n}_0 + Y_0(p)}\right\} = \pm 1 \Leftrightarrow \lim_{p\to\infty} Y_0(p) = 0 \text{ or } \infty \tag{11}$$

In our particular case, these mirrors must be positioned either side of the source at interface i, with progressive illumination from medium (i) for mirror M'_i, and retrograde illumination from medium (i+1) for mirror M_i (see Fig. 5, left). Hence their reflection coefficients write as [24]:

$$r'_i = \frac{\tilde{n}_i - Y'_i}{\tilde{n}_i + Y'_i} \text{ and } r_i = \frac{-\tilde{n}_{i+1} - Y_i}{-\tilde{n}_{i+1} + Y_i} \tag{12}$$

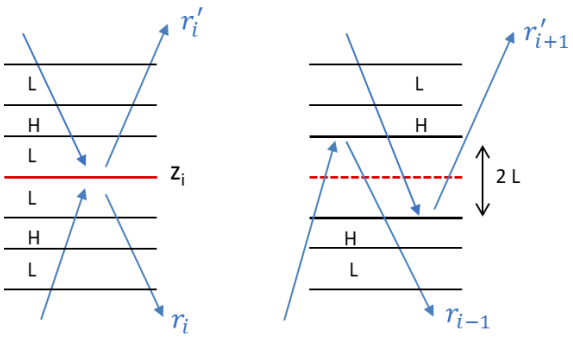

Fig. 5. To obtain asymptotically zero admittance either side of the source at interface i, the source must be located between 2 mirrors with positive reflection coefficients, i.e. starting with a layer of low refractive index (left figure). The resulting structure is a Fabry-Perot (right figure) comprising 2 negative reflection coefficient mirrors, i.e. starting with a layer of high refractive index. See text.

In order for each admittance to tend to zero, it is necessary that $r_i = r'_i = 1$, which leads to consider mirrors of type $(LH)^q L$ either side of the interface [24], where H and L designate high and low-index quarter-wave layers matched at the illumination wavelength and incidence. Since interface (i) is then necessarily situated between two media of the same low refractive index, these together constituting the median layer (known as a cavity or spacer), we finally end up with

Optics EXPRESS

a Fabry-Perot (Fig. 5, right) comprising 2 types $(HL)^q$ opposite facing mirrors, this time giving a negative reflection coefficient ($r_{i-1} = r'_{i+1} = -1$).

Hence, we get a classical result where we have used two mirrors to construct the Fabry-Perot structure whose formula is:

$$FP = superstrate\ (LH)^q 2L (HL)^q\ substrate \tag{13}$$

In Fig. 6 (right) the resonance conditions of this filter are designed for TE polarization at wavelength $\lambda^0 = 633nm$ and merging angle $\theta_0^0 = 0°$ in the end media. The superstrate is air ($n_0 = 1$) and the substrate is glass ($n_s = 1.52$). The thin film materials are Ta_2O_5 ($n_H = 2.15$) and SiO_2 ($n_L = 1.49$) at 633nm. The emission diagram of the structure is plotted in the incidence plane ($\varphi = 0°$) at wavelength $\lambda = \lambda^0$. The layer number is 25 (q = 6). The current is located at the center of the Fabry-Perot cavity. In order to emphasize the impact of the multilayer structure on the emission pattern, and to allow comparison with other results in the literature, we also plotted the emission pattern from a current at the top interface of a 13-layer mirror (Fig. 6, central figure). In addition, both patterns (mirror and Fabry-Perot) are normalized at each angle by the quasi-lambertian pattern (Fig. 6, left) emitted by a source at the center of a very thin (1nm) high-index layer cavity. Hence the enhancement is analyzed regarding that of the thin layer cavity. Its value approaches 40 in the Fabry-Perot cavity while it is around 4 in the mirror case. Note that we plotted in Fig. 6 an angular intensity pattern (or flux per unit of solid angle), while Eq. (1) is given for a power spectral density. The link between these 2 quantities can be found in [24,30,31,48].

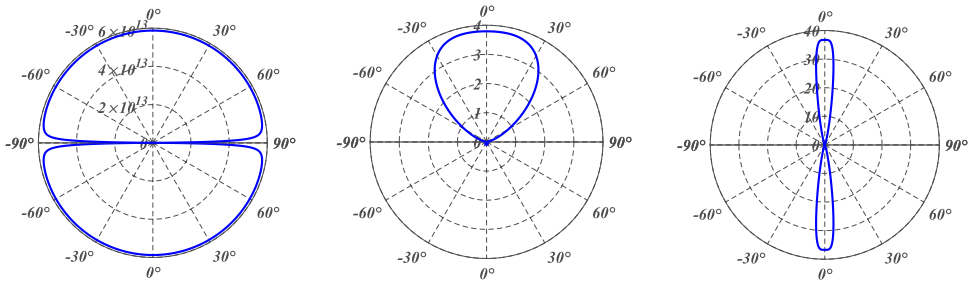

Fig. 6. Angular patterns at 633 nm for a single very thin layer cavity (left, SI units), for a 13 layer multi-dielectric quarter-wave mirror (central figure) of design $QW = L(HL)^6$, and for a 25-layer Fabry-Perot filter of design $(LH)^q\ 2L\ (HL)^q$. The central and right patterns are normalized to the left one (see text) at each angle. TE polarization.

To be complete, we also give the analytical expression of the power density $f^-(\vec{\sigma})$ emitted in the superstrate medium by the Fabry-Perot cavity. If the current is located in the middle of the cavity, we obtain following:

$$f^-(\vec{\sigma}) = 2\pi^2\sigma\ \frac{\tilde{n}_0\tilde{n}_S^2}{(\tilde{n}_0+\tilde{n}_S)^2\tilde{n}_L^2}\beta^{2q}\left|\hat{J}_c(\vec{\sigma})\right|^2 \tag{14}$$

Thus, the emission enhancement in free space is a power of the ratio $\beta = \tilde{n}_H/\tilde{n}_L$ of the effective indices $\tilde{n}_i$, and increases as a function of the number of layers in the structure. However, the field enhancement [24] mainly occurs in the median layer of the component (Fig. 7, left), which confers no sensitivity to substrate contamination. For that reason, these structures are not suitable for sensors. This problem will be resolved using the ZAL (Zero Admittance Layer) technique in the next section, allowing the second Fabry-Perot mirror to be dispensed with.

Optics EXPRESS

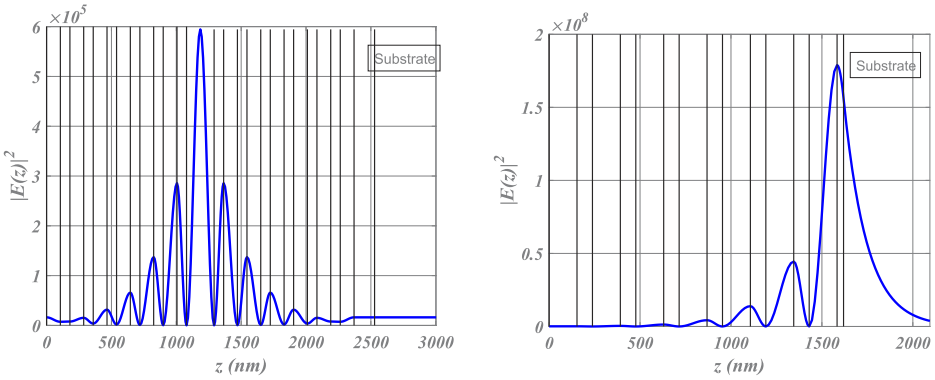

Fig. 7. Left figure is for the stationary electric field within the Fabry-Perot cavity of Fig. 6. Enhancement occurs in the median layer (no substrate sensitivity). Right figure is for the ZAL cavity of Fig. 9, under total reflection. Enhancement occurs in the substrate (high substrate sensitivity). In this calculation we considered a unit current ($|\hat{J}_c(\vec{\sigma})| = 1$) and TE polarization.

3. Optimization with the ZAL technique in the TIR regime

To ensure a field enhancement in the substrate we must look for another design technique. The basic idea lies on the fact that, since zero admittance means a unity reflection coefficient ($r = +1$), at least one multi-dielectric mirror could be replaced by total internal reflection (TIR) on the substrate interface. This leads us to consider the TIR regime where the phase of the TIR coefficient should be controlled (set to zero). To do that we can draw on the ZAL method [17] previously used for illumination in free space and based on the use of zero admittance layers. Indeed, we know that if the admittance cannot be zero in the free space window (unless asymptotically), it can, however, become zero at certain frequencies provided the total internal reflection (TIR) regime applies [17]. This has already enabled us to synthesize and control giant enhancements when the illumination comes from the far field of the surrounding media [12,17,19,24], and the question here is to know whether this technique remains valid in a micro-cavity configuration.

3.1. Cancelling the admittance on the substrate side

Actually (see Fig. 8, left) it is always possible to make admittance Y' vanish close to the substrate provided a thin film can be inserted there (known as a ZAL, i.e. zero admittance layer [19]) whose opto-geometric parameters satisfy the condition:

$$Y'_{p-1}(\sigma_m) = 0 \Leftrightarrow \tan\delta_p(\sigma_m) = -\frac{j\tilde{n}_s(\sigma_m)}{\tilde{n}_p(\sigma_m)} \tag{15}$$

where $\tilde{n}_s$ is the effective index of the substrate and $\tilde{n}_p$ is that of the ZAL layer, and where δ_p is a dimensionless phase term:

$$\delta_p = \left(\frac{2\pi}{\lambda}\right) n_p e_p \cos\theta_p \tag{16}$$

In Eq. (15), (16) the parameters for the ZAL layer are thickness e_p and refractive index n_p which can be chosen arbitrarily as n_L or n_H. The angle θ_i corresponds to the angle of propagation in layer i, with:

$$\sigma_m = k_i \sin\theta_i \tag{17}$$

Optics EXPRESS

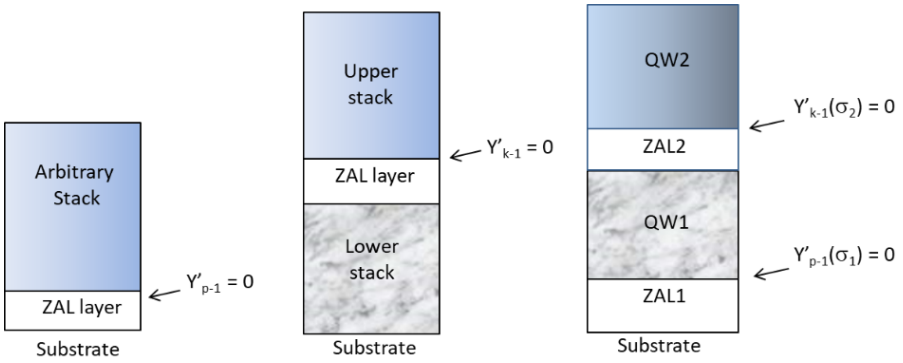

Fig. 8. Positioning of ZAL layers, at some arbitrary frequency, to make zero the admittance of a semi-infinite substrate (left figure) or that of a sub-stack (middle figure). In the figure on the right, the presence of 2 ZAL layers allows the admittance at frequencies σ_1 and σ_2 to be simultaneously zero.

To satisfy Eq. (15) one of the 2 effective indices must be pure imaginary, the other real. The TIR regime already ensures that the substrate effective index is imaginary, that is:

$$\sigma_m > k_s \Leftrightarrow \Re\{\tilde{n}_s\} = 0 \tag{18}$$

Note that the TIR condition Eq. (18) only depends on the substrate effective index; furthermore, following Eq. (17) it requires a high-index superstrate ($k_0 > k_s$). Then it remains to consider free-space emission in the superstrate ($\sigma_m < k_0$) to ensure a real effective index in all layers (including the superstrate and the ZAL layer), that is [19,24]:

$$\sigma_m = k_i \sin\theta_i < k_0 \Rightarrow \Im[\tilde{n}_i] = 0 \tag{19}$$

Note that this inequality Eq. (19) does not predetermine the positioning of $k_{L\ or\ H}$ with respect to k_0, and that it imposes that the field be trigonometric in nature within the volume of the stack, while it is evanescent in the substrate, that is:

$$k_s < \sigma_m < k_L < k_H \tag{20}$$

At this stage, it must be observed that only the admittance Y'_{p-1} (calculated from the effective index $\tilde{n}_s$ of the substrate) is zero, while Y_{p-1} (calculated from the effective index $-\tilde{n}_0$ of the superstrate) must also be zero. The same procedure cannot be used to make Y_{p-1} zero as we would end up with an inequality inconsistent with that given in Eq. (20), since it would describe a TIR regime for the 2 emergent media. Hence, we have to be content with an asymptotic pole for Y_{p-1}, requiring the introduction of a mirror. By analogy with the previous Fabry-Perot cavity, this means that one multi-dielectric mirror has been eliminated from the Fabry-Perot structure. Finally, the second mirror is provided by interface p in total reflection, with phase matching is guaranteed by the ZAL layer.

As for the previous Fabry-Perot structure, we can give an analytical expression for the power provided by a surface current in this ZAL cavity. If the current is located on the upper interface of the ZAL, we get for the pattern in the superstrate:

$$Y_{p-1}(\sigma_m) = -\frac{\tilde{n}_L^2}{\tilde{n}_0}\left(\frac{1}{\beta^{2q}}\right) = -\Delta Y_{p-1}(\sigma_m) \tag{21}$$

and hence:

$$f^-(\vec{\sigma}_m) = 2\pi^2 \sigma_m \frac{\tilde{n}_0}{\tilde{n}_L^2} \beta^{2q} \left|\hat{J}_{p-1}(\vec{\sigma}_m)\right|^2 \tag{22}$$

Optics EXPRESS

We again get a new enhancement in the form of a power of β^{2q} of the effective index ratio index β. Note that the main difference between expression Eq. (22) and expression Eq. (14) is that Eq. (22) is given for the pattern in the superstrate, while Eq. (14) concerns both the substrate and superstrate. Furthermore, due to the TIR regime the spatial frequency is higher in Eq. (22), which makes the index ratio β and then the ZAL enhancement much more intense.

3.2. Numerical calculation

In order to illustrate and validate this ZAL technique, we have plotted in Fig. 9 the angular pattern of a multilayer stack whose design is:

$$ZAL\ Cavity = Glass - L(HL)^q - ZAL - \ air \tag{23}$$

The stack is designed for TE polarization in the TIR regime, for wavelength $\lambda^0 = 633nm$ and merging incidence $\theta_0^0 = 45°$ in the superstrate medium. The current is located at the top surface of the ZAL layer (interface p-1 = 13 with q = 6). The thin film materials are those of Fig. 6, while the superstrate and substrate are glass ($n_s = 1.52$) and air ($n_0 = 1.$) respectively. The ZAL layer is a L layer with a thickness of 35.603 nm. The emission pattern is plotted for TE polarization at wavelength $\lambda = \lambda^0$ in the incidence plane ($\varphi = 0°$) in the superstrate.

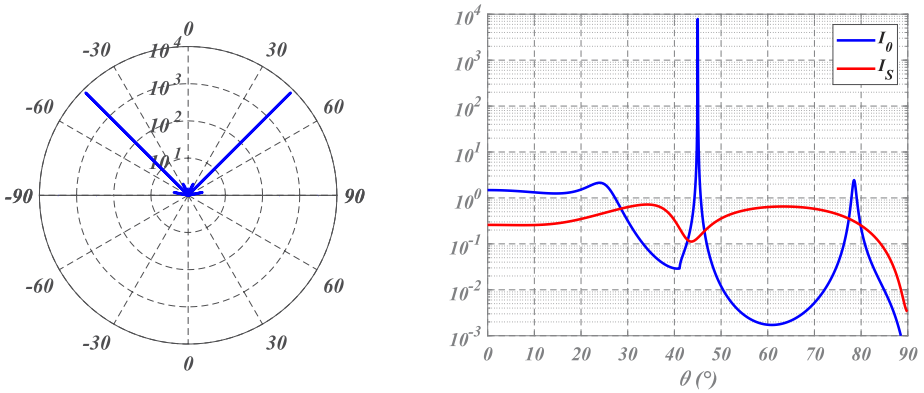

Fig. 9. TE normalized angular pattern at 633 nm of the ZAL micro-cavity plotted in polar (left figure) and cartesian (right figure) coordinates. I_0 and I_S are given for the patterns in the superstrate (blue curve) and substrate (red curve).

According to (22), the cavity is expected to enhance the TE-polarized source emission in the superstrate at the observation parameters (λ^0, θ_0^0). This is indeed what we observe in Fig. 9 since there is an intense peak at 45° with four decades enhancement. Note also the narrow angular width $\Delta\theta_0$ of the peak, where most of the energy is concentrated; the percentage of energy in the peak is 14% for $\Delta\theta_0 = 0.01°$ and 36% for $\Delta\theta_0 = 0.1°$. These values must be multiplied by a factor of 2 because of the symmetrical peak. Recall that the peak amplitude and width are respectively proportional and inversely proportional to the number of layers. Other peaks are present but cannot be seen in the left-hand figure because their amplitude is several decades smaller. They can be seen on the right-hand figure where the pattern is plotted both in the superstrate (blue curve) and in the substrate (red curve).

Consequently, at this step there are several advantages to the ZAL coating. One is technological since one of the two mirrors is eliminated and replaced by a single thin layer; hence the deposition time is reduced, as are the in-situ control difficulties of the deposition process [20,23]. Another advantage is related to the fact that the enhancement can be designed at arbitrary wavelengths, angles and polarization modes (see next section). We will also show in the next section how

Optics EXPRESS

simultaneous resonances can be designed. Eventually the last advantage is a major one for sensor applications: in the case of the ZAL cavity, the integral of the field within the substrate is very large and leads to a huge sensitivity to any contamination in this substrate (see Fig. 7), which was not the case for the previous Fabry-Perot cavity. The sensitivity of the ZAL structure is analyzed in section 5.

We finish this section by plotting the wavelength variations of the ZAL cavity in the immediate neighborhood of resonance. As illustrated in Fig. 10 (left), we go from strong enhancement to strong inhibition depending on whether the current is located on the upper interface of the ZAL layer (interface 13) or on the component's first interface (interface 0). This is related to the fact that the pole of the difference in admittance ΔY is asymptotic and not exact. We also show in Fig. 10 (right) how putting the ZAL structures in series in the form $(QW/ZAL)^n$ enables steeper rising fronts to be constructed; this way of proceeding is similar to that for multi-cavity narrow band filters [20,21,23]. Note here that in the $(QW/ZAL)^n$ structure, the source is unique and located on the penultimate interface of the stack. At this step there is no upper bound on the enhancement which increases with the layer number; this will be discussed in section 5.

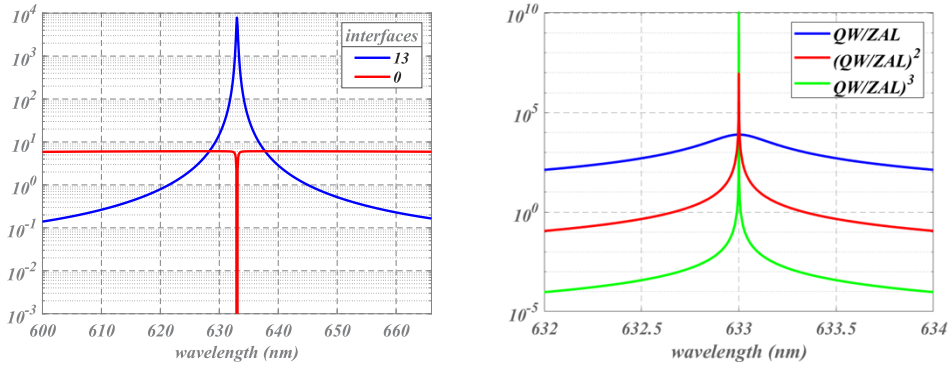

Fig. 10. TE wavelength variations at 45° of the reflected pattern of the QW/ZAL cavity (left side), for a current localized at the top interface of the ZAL layer (#13, blue curve), or at the top interface of the multilayer (#0, red curve). The right-hand figure is given for ZAL cavities in series in the form $(QW/ZAL)^2$ and $(QW/ZAL)^3$.

4. Designing the cavity for multiple resonances

We now turn our attention to a more general analysis of the spectral and angular behavior of the ZAL structure. If we maintain the previous QW/ZAL structure, we obtain the variations illustrated in Fig. 11, where a mapping for angle and wavelength is given. The bright line on the right figure between 75° and 85° is not significant, as illustrated by the modest levels shown on the left and right figures. On the other hand, the quasi-vertical resonance line around 45°, characteristic of the presence of a pole, can clearly be seen. This line results from the fact that Eq. (15) leads to a set of solutions when the parameters (λ, θ) vary, guaranteeing that Y'_{p-1} vanishes. Rigorously speaking, the enhancement ought to diminish or disappear on account of dispersion of the admittance difference; however, this is negligible over the domain plotted. In a classical sense, and similarly to that of the Fabry-Perot cavities, we can also increase the thickness of the spacer since equation Eq. (15) allows several solutions modulo π, i.e. $n_p e_p^k cos\theta_p = k\lambda_0/2$, with harmonics appearing as illustrated in Fig. 12.

However, these results do not allow arbitrary control over the spectral or angular variations of the resonances, though it could be important to know how to generate simultaneously several angular or spectral resonances at arbitrarily imposed frequencies. This type of synthesis has already

Optics EXPRESS

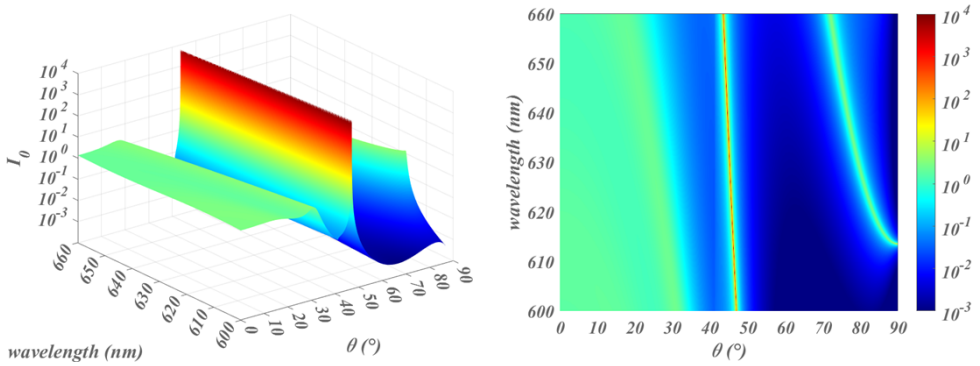

Fig. 11. Mapping the enhancement as a function of angle and wavelength for a ZAL cavity (TE polarization).

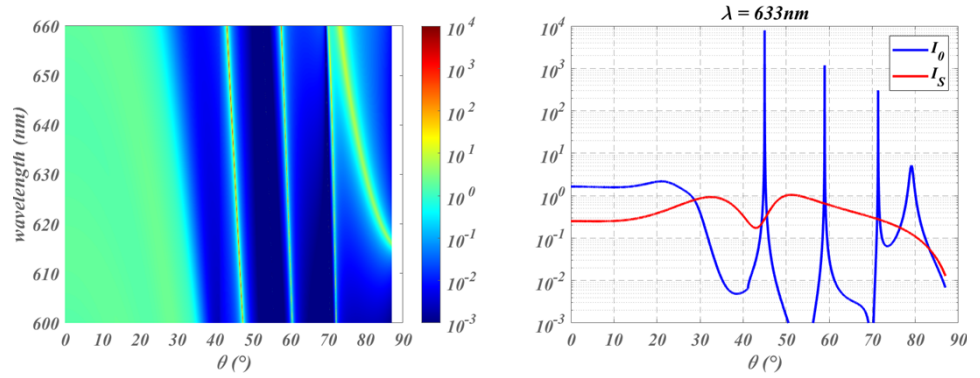

Fig. 12. Structure identical to Fig. 11, but with a thicker ZAL layer modulo 2π (k = 2). See text.

been carried out for free space [17], and the question arises as to whether these simultaneous resonances can also be controlled in a micro-cavity.

The basic idea rests on the fact that Eq. (15) can be generalized to a sub-stack of admittance Y'_k that would replace the substrate (see Fig. 8, middle diagram). In this case the parameters of the ZAL layer (numbered k) that cause the admittance at interface k-1 to vanish are given by:

$$Y'_{k-1}(\sigma_m) = 0 \Rightarrow \tan\delta_k(\sigma_m) = -\frac{jY'_k(\sigma_m)}{\tilde{n}_k(\sigma_m)} \tag{24}$$

Equation (24) is similar to Eq. (15), except that the substrate effective index has been replaced by the admittance of the sub-stack. Note that in order for δ_k to be real in Eq. (24), admittance Y'_k must be imaginary. For that it is sufficient that the effective index $\tilde{n}_s$ of the substrate, from which admittance Y'_k is calculated by recurrence, is imaginary [17,24]. Indeed, we have:

$$\Re\{\tilde{n}_s\} = 0 \Rightarrow \forall z \;\; \Re\{Y'(z)\} = 0 \tag{25}$$

As before, this observation means that the regime has to be one of total reflection on the substrate at angular frequency σ_m; this corresponds to our investigation.

Property Eq. (24) introduces several degrees of freedom. Actually, the ZAL layer now separates the component into 2 multilayer substructures, namely an upper part S_2 ($i<k-1$) deposited onto a multilayer substrate of zero admittance Y'_{k-1} and a lower, arbitrary, part S_1 ($i>k-1$). At angular

Optics EXPRESS

frequency σ_m the 2 substructures are somewhat independent: classically speaking, we know that, before normalization, the distribution of the stationary field within the lower stack S_1 does not depend [20,24] on the upper stack S_2; furthermore, given that the admittance is specified at interface k-1, then that of the upper stack S_2 is also independent of the lower stack S_1. In all cases, the association of the 2 sub-stacks will lead to a resonance at frequency σ_m, provided that the other admittance Y_{k-1} tends to zero. This technique allows, for example, the field maximum to be drawn away from the substrate interface. The technique is also very useful when one wants to excite a source that is already in the form of a multilayer sub-stack [30,31].

Based on this observation, we can imagine designing a double structure (Fig. 8, right) resonating at 2 imposed pulsations σ_1 and σ_2. The lower stack is designed to resonate at σ_1 on account of the ZAL1 layer (numbered p), which ensures the condition $Y'_{p-1}(\sigma_1) = 0$, onto which is deposited the quarter-wave mirror $QW1$. Onto this component $QW1/ZAL1$ is then deposited a second ZAL2 layer (numbered k) that causes the admittance at frequency σ_2 to vanish, i.e. $Y'_{k-1}(\sigma_2) = 0$. A second quarter-wave mirror $QW2$ covers this ZAL2 layer so that the $QW2/ZAL2$ structure creates a resonance at frequency σ_2.

4.1. Enhancement at 2 wavelengths

Numerical results are given in Fig. 13 (left) for a double ZAL structure of the form $QW2/ZAL2/QW1/ZAL1$ designed to create an enhancement at wavelengths $\lambda_1 = 633$nm and $\lambda_2 = 613$nm, in TE polarization in the 45° direction. The blue curve (I_{z1}) corresponds to the case where the source is on the upper interface of the ZAL1 layer. It shows 2 strong enhancements around λ_1 and λ_2, with a higher value at λ_1. Similarly, the red curve (I_{z2}) corresponds to the case where the source is on the upper interface of the ZAL2 layer, and also shows 2 strong enhancements at λ_1 et λ_2, with a higher value at λ_2. By way of reference, the dotted green curve is shown, which corresponds to the original $QW1/ZAL1$ stack, supposedly resonating only at frequency σ_1. These first results show that the multiple ZAL cavity can be designed to control enhancement at 2 simultaneous frequencies.

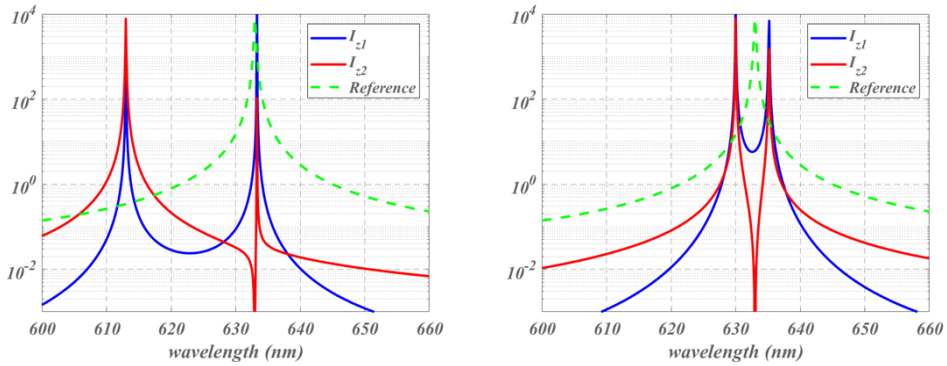

Fig. 13. A double ZAL structure designed to resonate at 2 wavelengths (see text).

While these results may be particularly convincing, a slight spectral shift can be seen with respect to the expected wavelengths. To observe this phenomenon better, we have done the same calculations again using wavelengths that are closer together, i.e. $\lambda_1 = 633$nm and $\lambda_2 = 630$nm. The results are shown in Fig. 13 (right) and confirm the slight spectral shift. This is explained by the spectral dispersion in the phase of the reflection coefficient of the wide-band mirror whose formula is $QW2/ZAL2/QW1$. With the structure on the right of Fig. 8, resonance is always assured exactly at λ_2, since the ZAL2 layer guarantees that the admittance Y'_{k-1} will vanish at σ_2, and that it is over-coated by a QW2 positive reflection coefficient mirror (r = +1). The

Optics EXPRESS

situation is different for the resonance at λ_1 since, if the ZAL1 layer is properly deposited onto a zero admittance substrate ($Y'_{p-1}(\sigma_1) = 0$), the $QW2/ZAL2/QW1$ mirror that covers it is no longer a quarter wavelength mirror at λ_1, so its reflection factor is not necessarily real. This is a reminder that the reflection coefficient must be real (positive) to maximize the enhancement, which is guaranteed only at the central wavelength λ_{QW} of a quarter-wave mirror. Hence, the phase dispersion of the $QW2/ZAL2/QW1$ mirror reduces, or slightly shifts, the enhancements, as observed in Fig. 13.

4.2. Mixing angular and wavelength resonances

Using this technique, it is also possible to mix an angle resonance with a wavelength resonance, which means that the angle is different for each wavelength. This is illustrated in Fig. 14, which shows the angular emission pattern for a QW2/ZAL2/QW1/ZAL1 structure whose ZAL layers have been constructed to obtain resonances at $(\lambda_1^0, \theta_1^0) = (633nm,\ 45°)$ and $(\lambda_2^0, \theta_2^0) = (613nm, 60°)$. As expected, the enhancement approaches 4 decades at 633 nm and 45°, while it exceeds two decades at 613 nm and 60°. Such procedure can also be used to design simultaneous resonances at different polarizations.

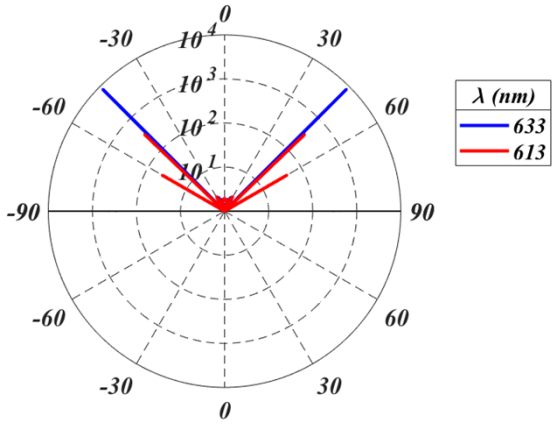

Fig. 14. Structures designed to resonate at 2 wavelengths and at 2 different emission angles, i.e. $(\lambda_1, \theta_1) = (633nm,\ 45°)$ and $(\lambda_2, \theta_2) = (613nm, 60°)$. See text.

4.3. Generalization to several wavelengths

These techniques can be generalized to a greater number of wavelengths, as illustrated in Fig. 15 (left). In this figure the component is designed to generate 9 resonances at wavelengths of 610nm, 620nm, 630nm, 640nm, 650nm, 660nm, 670nm, 680nm and 690nm. Its formula is Glass/$(QWZAL)^9 \ldots (QWZAL)^2(QWZAL)^1$/Air. The source is unique and located on the upper ZAL1 interface close to the substrate. We observe in Fig. 15 (left) that the enhancement peaks are properly positioned despite the mirrors' phase dispersion, and that the first 5 resonances are very pronounced ($\geq 10^5$). We can point out at this stage that each ZAL is designed to support a current on its upper interface, while the stack contains just a single source. This is the reason why the enhancement is reduced at the last 4 wavelengths ($\geq$ 660nm).

In order to check that point we have plotted on Fig. 15 (right) the response of the same component where each of the ZAL layer supports a current. From a technological point of view, this means that the stack contains several luminescent layers. The results then show that almost all the resonances are retained with powerful enhancements. It will be noted that the possibility of resonances at several wavelengths might be very useful for micro-source applications; in

Optics EXPRESS

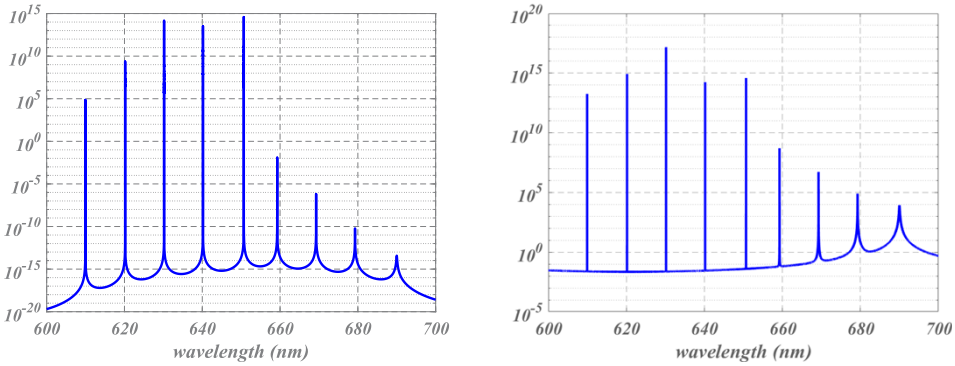

Fig. 15. A multi-ZAL structure designed to resonate at 9 wavelengths (see text). The component contains a single source (left) or several sources (right).

particular, if the source has to be activated optically at λ_1, an enhancement can be imposed at this pump wavelength λ_1; then a second wavelength λ_2 can be chosen to exalt the pattern at λ_2, leading to a multiplicity of the enhancement.

5. Limits and sensitivity study

It remains to check that these structures remain extremely sensitive to contamination of the substrate. Since we saw in the previous sections that the emission enhancement is proportional to a power β^{2q} of the effective index ratio β, one might think that the higher the layer number ($p = 2q+1$), the better the efficiency. Actually the enhancement process is more complex and requires a detailed investigation. We will start with the enhancement limits.

5.1. Enhancement limits

We previously stressed on the fact that, while the enhancement increases with the layer number p, its angular bandwidth $\delta\theta(p)$ decreases with this number. Hence for large p values, any receiver will integrate the micro-cavity pattern in its angular aperture, leading to a power integral responsible for the enhancement limit. Let us focus on this integral over the bandwidth $\delta\theta(p)$, and assume that the admittance difference $\Delta Y_i(p)$ contains a zero $\chi_m(p)$ of order 1, that is:

$$\Delta Y_i(\sigma, p) = C(\sigma, p)[\sigma - \chi_m(p)] \quad \text{with} \quad \chi_m = \chi_m^{'} + j\chi_m^{''} \tag{26}$$

Following section 2, this zero $\chi_m(p)$ is necessarily complex and tends to the real resonance frequency σ_m for large p values (see Eq. 10). According to Eq. (1) the integral of the spectral power density over the bandwidth $\delta\theta$ therefore writes as:

$$\frac{\mathrm{dF}}{\mathrm{d}\varphi}(\chi_m^{'}, \varphi, p) = \Re[I(p)] = \Re\left[\frac{2\pi^2}{C(p, \chi_m^{'})}|\hat{J}_i(\chi_m^{'}, \varphi)|^2 I_0(p)\right] \tag{27}$$

with:

$$I_0(p) \approx \int_{\chi_m^{'} - \frac{\Delta\sigma}{2}}^{\chi_m^{'} + \frac{\Delta\sigma}{2}} \left[\frac{\sigma}{\sigma - \chi_m(p)}\right] d\sigma \tag{28}$$

In Eqs. (27)–(28) we neglected the variations of C and $\hat{J}_i$ over the narrow bandwidth $\delta\theta$ which asymptotically tends to zero. The last integral $I_0(p)$ can be calculated analytically:

$$I_0(p) = \eta(p)\chi_m^{''}(p) + j2\chi_m(p)\arctan\frac{\eta(p)}{2} \Rightarrow \lim_{p\to+\infty} I_0(p) = 2j\sigma_m \arctan\frac{\eta_\infty}{2} \tag{29}$$

Optics EXPRESS

where η is a proportionality factor between the imaginary pole $\chi_m^{''}$ and the frequency width $\Delta\sigma$ related to $\delta\theta$:

$$\eta(p) = \frac{\Delta\sigma(p)}{\chi_m^{''}(p)} \Rightarrow \eta_\infty = \lim_{p\to+\infty}\left\{\frac{\Delta\sigma(p)}{\chi_m^{''}(p)}\right\} \tag{30}$$

Eventually we get:

$$\lim_{p\to+\infty}\frac{dF}{d\varphi} = 4\pi^2\sigma_m \arctan\left(\frac{\eta_\infty}{2}\right)\frac{\Im[C_\infty(\sigma_m)]}{|C_\infty(\sigma_m)|^2}\left|\hat{J}_i(\chi_m', \varphi)\right|^2 \tag{31}$$

with:

$$C_\infty(\sigma_m) = \lim_{p\to+\infty}[C(p, \sigma_m)] \tag{32}$$

Note that the C coefficient shows slight dependence versus p above a certain (and low) value, so that Eq. (31) proves the convergence integral and emphasizes the enhancement limit of the ZAL micro-cavity pattern. Also note that $\Im[C_\infty(\sigma_m)] \neq 0$, due to the fact that in the admittance difference ΔY_i (see Eq. (26)), $Y_i^{'}$ is purely imaginary (due to the TIR regime) and Y_i is real (due to the central wavelength of the matched mirror- see Eq. (12)).

Though this proof can be generalized to the mth order poles of the scattering power density, we checked these results numerically in Fig. 16. The cavity design is the same than that of Fig. 10 (left) but we used different layer numbers for the quarter-wave mirror. The left figure shows the increase of emission pattern at resonance, together with the decrease of the angular bandwidth $\delta\theta$, for 3 layer numbers (5, 13 and 21). In the right figure we plotted the integral of the emission pattern, which is the quantity recorded (measured) by the receiver. Integration is performed between 44° and 46°, and the quantity obtained is normalized by the integral of the emission pattern of the very thin layer cavity of Fig. 6 over the same angular range. As expected, we observe a stationary value (around 93 times the power emitted by a very thin layer cavity) of the power above 15 layers. This is a key result which would lead the manufacturer to use a moderate layer number, and not to expect unrealistic enhancement.

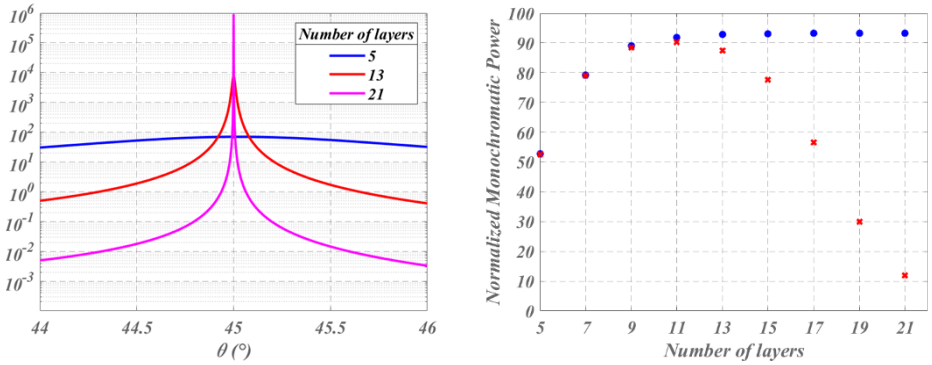

Fig. 16. Angular pattern of the transparent ZAL cavity (left figure) for 3 different layer numbers. The right figure is for the same pattern integrated in the angular range 44°<θ<46° and plotted versus the layer number, for a transparent cavity (blue dots) and for imaginary indices of 10^{-5} (red crosses). Data are normalized in regard to the thin layer cavity of Fig. 6 (see text).

It should be stressed that Eq. (31) is for an intrinsic limit of a transparent micro-cavity. However another limit may originate from absorption. Indeed despite the low imaginary indices of dielectric layers (around 10^{-5}), absorption cannot be neglected in regard to the high field values (proportional to β^{2q}) in the vicinity of the ZAL interface. This is why we plotted another flux pattern in Fig. 16 (right figure) for the same cavity but involving an imaginary index of 10^{-5}

Optics EXPRESS

for all layers. We first observe that a maximum is attained for 11 layers, and then that the power decreases above this value. This is again a major result which now means that the layer number must be adjusted, since there is a limit not to exceed. The enhancement again is around 90.

So far, we have shown that the amount of power reaching a receiver is limited as the number of layers increases. One would also wonder if the electric field in the structure tends toward infinity as the number of layers increases. This is a priori the case for a transparent cavity, since the field plotted in Fig. 7 diverges as β^{2q} with the layer number. However one cannot forget that the quantity plotted in Fig. 7 is related to the electric field in the spatial Fourier plane [24]. To get the physical electric field, one needs to compute the inverse Fourier transform versus the spatial pulsation $\vec{\sigma}$, that is [24]:

$$E(\vec{r}, z) = \int_{\vec{\sigma}} \hat{E}(\vec{\sigma}, z) e^{j\vec{\sigma}.\vec{r}} d^2\vec{\sigma} \tag{33}$$

The square modulus $|E(\vec{r}, z)|^2$ of this physical field is plotted in Fig. 17 as a function of the layer number. For the sake of simplicity, the field is taken at $\vec{r} = \vec{0}$, so that Eq. (33) reduces to the integral of the electric field calculated in the spatial Fourier plane. Furthermore, the integration range is limited to the angular range $44° < \theta < 46°$ where the enhancement occurs. Finally, the electric field is computed at the z altitude where it reaches a maximum, so at the top surface of the ZAL layer (see Fig. 7). As expected, the maximum value of the electric field is bounded when the layer number increases (see Fig. 17).

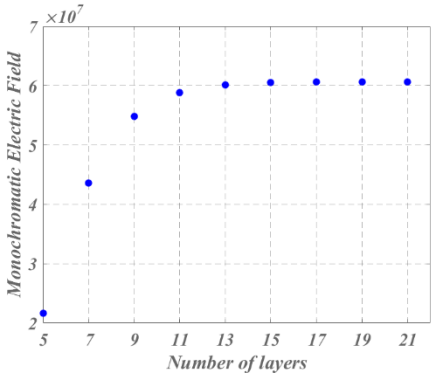

Fig. 17. Square modulus of the physical electric field (see text) plotted versus the layer number, for a transparent ZAL cavity. The field is calculated at the top surface of the ZAL layer for a unit current modulus ($|\hat{J}_c(\vec{\sigma})| = 1$).

Eventually, strictly speaking one would also consider another ultimate limit which is the accuracy of the cavity design. Indeed, this accuracy increases with the layer number, so that each layer thickness would be perfectly controlled in the manufacturing process [20–23]. However, with this limited layer number (p = 11) we have checked that this is not a difficulty.

5.2. Sensitivity

We now come to the sensitivity. Actually, this sensitivity is not directly related to the emission enhancement, but to the spectral or angular shift of the emission pattern in response to a substrate contamination. In other words, the key parameter is the derivative of the pattern versus the refractive index of substrate. We already know that this derivative is optimized in the sense that the field enhancement primarily occurs in the contaminated medium, i.e. in the substrate (here air or liquid). This represents a major difference as compared with Fabry-Perot filters, for which the enhancement occurs between 2 multilayer mirrors (hence far from the substrate), thus destroying their sensitivity to contamination of the substrate.

Optics EXPRESS

In the interests of clarity and to allow easy comparison with other techniques, 2 types of contamination are distinguished. In the first case we assume that the substrate is uniformly contaminated, such that it gives rise to a variation Δn_s of refractive index, which alters the cavity's emission pattern. In the second case, it is the optical thickness of the last working layer that is altered by a value $\Delta(ne)$; note that, rigorously speaking, a functional layer must be added to the luminescent layer, and that the ZAL must be adjusted as a consequence.

The numerical calculation of sensitivity is given in Fig. 18, which shows how the resonance shifts with wavelength ($\Delta\lambda$) in both these contamination cases. Following the previous sub-section 6.1, we chose a single ZAL cavity to limit the layer number. The design is that of Fig. 10 (left) except that the imaginary indices are 10^{-5} (not zero). We observe that variations of 10^{-4} in Δn_s or $\Delta(ne)$ give rise to a wavelength shift of 0.035 nm and 0.102 nm respectively, i.e. an approximate average sensitivity of $\frac{\Delta n_s}{\Delta\lambda} = 2.86\ 10^{-3} nm^{-1}$ and $\frac{\Delta(ne)}{\Delta\lambda} = 9.80\ 10^{-4}\ nm^{-1}$

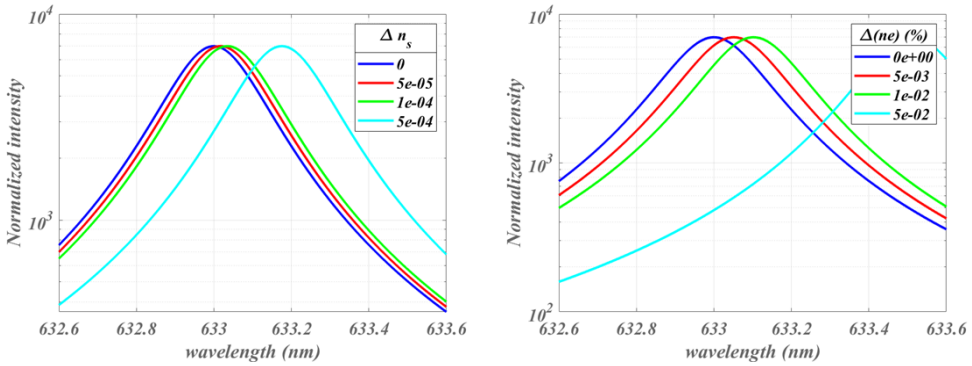

Fig. 18. Spectral variation generated by an alteration of index Δn_s of the substrate (left figure), or of the optical thickness (right figure) of a functional layer Δ(ne). The design is a single ZAL.

The detectability (the smallest measurable value of Δn_s) will ultimately depend on the performance (including cost and size) of the spectrophotometer implemented to measure the spectral profile of the light flux provided by the optical fiber. Recall that, using for example a holographic grating of 1800 lines/mm and an effective focal length of about 200 mm, the linear dispersion obtained in the focal plane of this device will be of the order of 2 nm/mm, i.e. a sampling every 0.05 nm if the focal plane carries an array of photodiodes with a pitch of 26 µm; this means that the spectral profile (1nm width) plotted in see Fig. 18 will be dispersed over typically 20 photodiodes. If we assume that the noise is determined by the contribution of the shot noise (for a low-noise scientific camera, this will always be the case if the integration time is properly adjusted), simple simulations show that the smallest spectral shift of the barycenter that can be detected will be better than one tenth of the pixel sampling step, i.e. 5 pm: this would lead to a minimum Δn_s of about 10^{-5}.

6. Conclusion

Our objective was to see whether our analytical techniques for synthesizing giant field enhancements, developed for amorphous (passive) multilayer systems illuminated in free space [17], could be generalized to micro-cavities containing at least one luminescent layer (active crystalline, activated electrically or optically) in the TIR regime. All results were shown successful, which means that resonances in multilayer micro-cavities can be designed and optimized at arbitrary angles, wavelengths and polarizations. The possibility of multiple simultaneous resonances was

Optics EXPRESS

also demonstrated. In a more general way, such issues might motivate more studies devoted to the design of multilayers under the TIR regime.

The origins of enhancement limits were analyzed in detail. It was shown that, though the local pattern (at one angle) of a transparent cavity increases indefinitely (by several decades) with the layer number, the measurable pattern (integrated over the narrow angular bandwidth of the resonance) remains bounded and lower than 100 (compared to the pattern of a very thin single layer cavity). Slight imaginary indices were also considered to show that there was an optimum layer number to be achieved but not to be exceeded. This may constitute a major result for manufacturers.

All the coatings were designed under the TIR regime and exhibit field enhancement in the substrate, which confers high sensitivity to substrate contamination (in opposition to classical Fabry-Perot structures). Hence these components are well suited to sensor applications and provide a useful alternative to existing all-dielectric sensors used under free-space illumination. Indeed with these micro-cavity sensors we dispense with both the illumination (which was removed) and the pixel matrix detector (which was replaced by an optical fiber connected to a spectrophotometer). This demonstrated the advantages of a micro-cavity sensor, simpler to implement (no tuning of the illumination band-passes) and taking up considerably less space. As usual, experiment remains to be done and is in progress.

Acknowledgments. We acknowledge the joint laboratory (LabTop) which gathers CILAS ArianeGroup and Institut Fresnel for interesting discussions.

Disclosures. The authors declare no conflicts of interest.

Data availability. No data were generated or analyzed in the presented research.

References

1. Jacob Fraden, "Handbook of Modern Sensors: Physics, Designs, and Applications", Springer-Verlag New York, Inc. 2004, ISBN 978-1-4419-6465-6
2. Roger G. Jackson, "*Novel Sensors and Sensing*", CRC Press, 2019, ISBN 9780367454319
3. Khaled Chetehouna, "*Volatile Organic Compounds: Emission, Pollution and Control*", Nova Science Publishers, 2014, ISBN: 978-1-63117-862-7
4. Stefan Alexander Maier, "*Plasmonics: Fundamentals and Applications*", Springer (2007), ISBN 9780387331508
5. . Cesaire Ndiaye, Fabien Lemarchand, Myriam Zerrad, Dominique Ausserré, and Claude Amra, "Optimal design for 100% absorption and maximum field enhancement in thin-film multilayers at resonances under total reflection," Appl. Opt. **50**(9), C382–C387 (2011).
6. A. Sinibaldi, N. Danz, E. Descrovi, P. Munzert, U. Schulz, F. Sonntag, L. Dominici, and F. Michelotti, "Direct comparison of the performance of Bloch surface wave and surface plasmon polariton sensors," Sensors and Actuators B: Chemical **174**, 292–298 (2012).
7. P. N. Melentiev, A. E. Afanasiev, A. A. Kuzin, A. S. Baturin, and V. I. Balykin, "Giant optical nonlinearity of a single plasmonic nanostructure," Opt. Express **21**(12), 13896–13905 (2013).
8. F. Michelotti, A. Sinibaldi, P. Munzert, N. Danz, and E. Descrovi, "Probing losses of dielectric multilayers by means of Bloch surface waves," Opt. Lett. **38**(5), 616–618 (2013).
9. A. Sinibaldi, R. Rizzo, G. Figliozzi, E. Descrovi, N. Danz, P. Munzert, A. Anopchenko, and F. Michelotti, "A full ellipsometric approach to optical sensing with Bloch surface waves on photonic crystals," Opt. Express **21**(20), 23331–23344 (2013).
10. Xiaoyuan Lu, Rengang Wan, Guoxi Wang, Tongyi Zhang, and Wenfu Zhang, "Giant and tunable electric field enhancement in the terahertz regime," Opt. Express **22**(22), 27001–27006 (2014).
11. Zouheir Sekkat, Shinji Hayashi, Dmitry V. Nesterenko, Anouar Rahmouni, Siham Refki, Hidekazu Ishitobi, Yasushi Inouye, and Satoshi Kawata, "Plasmonic coupled modes in metal-dielectric multilayer structures: Fano resonance and giant field enhancement," Opt. Express **24**(18), 20080–20088 (2016).
12. M. Zerrad, A. L. Lereu, C. N'diaye, F. Lemarchand, and C. Amra, "Bandwidths limitations of giant optical field enhancements in dielectric multi-layers," Opt. Express **25**(13), 14883–14891 (2017).
13. F. Michelotti, R. Rizzo, A. Sinibaldi, P. Munzert, C. Wächter, and N. Danz, "Design rules for combined label-free and fluorescence Bloch surface wave biosensors," Opt. Lett. **42**(14), 2798–2801 (2017).
14. P. Munzert, N. Danz, A. Sinibaldi, and F. Michelotti, "Multilayer coatings for Bloch surface wave optical biosensors," Surf. Coat. Technol. **314**, 79–84 (2017).
15. A. Occhicone, A. Sinibaldi, F. Sonntag, P. Munzert, N. Danz, and F. Michelotti, "A novel technique based on Bloch surface waves sustained by one-dimensional photonic crystals to probe mass transport in a microfluidic channel," Sensors and Actuators B: Chemical **247**, 532–539 (2017).

Optics EXPRESS

16. Shuomin Zhong, Taijun Liu, Jifu Huang, and Yungui Ma, "Giant power enhancement for quasi-omnidirectional light radiation via ε-near-zero materials," Opt. Express **26**(3), 2231–2241 (2018).
17. C. Amra, M. Zerrad, F. Lemarchand, A. Lereu, A. Passian, J. Antonio Zapien, and M. Lequime, "Energy density engineering via zero admittance domains in all-dielectric stratified materials," Phys. Rev. A **97**(2), 023819 (2018).
18. Q. Ren, J. W. You, and N. C. Panoiu, "Giant enhancement of the effective Raman susceptibility in metasurfaces made of silicon photonic crystal nanocavities," Opt. Express **26**(23), 30383–30392 (2018).
19. D. Niu, M. Zerrad, A. Lereu, A. Moreau, J. Lumeau, J. A. Zapien, A. Passian, V. Aubry, and C. Amra, "Excitation of Bloch Surface Waves in Zero-Admittance Multilayers for High-Sensitivity Sensor Applications," Phys. Rev. Applied **13**(5), 054064 (2020).
20. H. A. Macleod, *Thin-Film Optical Filters*, 4th ed, Series in Optics and Optoelectronics, CRC Press/Taylor & Francis (2010).
21. Alfred Thelen, *Design of Optical Interference Coating* (McGraw-Hill, 1989)
22. S.A. Furman and A.V. Tikhonravov, *Basics of Optics of Multilayer Systems* (World Scientific Publishing Co Pte Ltd, 1996)
23. Philip W. Baumeister, *Optical Coating Technology* (SPIE Publications, 2004)
24. C. Amra, M. Lequime, and M. Zerrad, *Electromagnetic Optics of Thin-Film Coatings: Light Scattering, Giant Field Enhancement, and Planar Microcavities*, Cambridge University Press (2021).
25. W. Lukosz and R. E. Kunz, "Light emission by magnetic and electric dipoles close to a plane dielectric interface. II. Radiation patterns of perpendicular oriented dipoles," J. Opt. Soc. Am. **67**(12), 1615–1619 (1977).
26. G. Björk, S. Machida, Y. Yamamoto, and K. Igeta, "Modification of spontaneous emission rate in planar dielectric microcavity structures," Phys. Rev. A **44**(669), 669–681 (1991).
27. D. G. Deppe and C. Lei, "Spontaneous emission from a dipole in a semiconductor microcavity," J. Appl. Phys. **70**(7), 3443–3448 (1991).
28. Elias Burstein and Claude Weisbuch, *Confined Electrons and Photons: New Physics and Applications*, Springer, (1995).
29. Edward Mills Purcell, "Spontaneous emission probabilities at radio frequencies," *Confined Electrons and Photons.* Springer, Boston, MA. 839, (1995)
30. C. Amra and S. Maure, "Electromagnetic power provided by sources within multilayer optics: free-space and modal patterns," J. Opt. Soc. Am. A **14**(11), 3102–3113 (1997).
31. C. Amra and S. Maure, "Mutual coherence and conical pattern of sources optimally excited within multilayer optics," J. Opt. Soc. Am. A **14**(11), 3114–3124 (1997).
32. S. Ciancaleoni, P. Mataloni, O. Jedrkiewicz, and F. De Martini, "Angular distribution of the spontaneous emission in a planar dielectric dye microcavity," J. Opt. Soc. Am. B **14**(7), 1556–1563 (1997).
33. H. Rigneault, S. Maure, and C. Amra, "Spontaneous emission in multilayer microcavities: modal theory extended with Fourier-Green analysis for dissipative structures," Pure Appl. Opt. **7**(3), 549–563 (1998).
34. H. Benisty, H. De Neve, and C. Weisbuch, "Impact of planar microcavity effects on light extraction-Part I: basic concepts and analytical trends," IEEE J. Quantum Electron. **34**(9), 1612–1631 (1998).
35. H. Benisty, H. De Neve, and C. Weisbuch, "Impact of planar microcavity effects on light extraction-Part II: selected exact simulations and role of photon recycling," IEEE J. Quantum Electron. **34**(9), 1632–1643 (1998).
36. H. Benisty, R. Stanley, and M. Mayer, "Method of source terms for dipole emission modification in modes of arbitrary planar structures," J. Opt. Soc. Am. A **15**(5), 1192–1201 (1998).
37. K. A. Neyts, "Simulation of light emission from thin-film microcavities," J. Opt. Soc. Am. A **15**(4), 962–971 (1998).
38. L. Polerecký, J. Hamrle, and B. D. MacCraith, "Theory of the radiation of dipoles placed within a multilayer system," Appl. Opt. **39**(22), 3968–3977 (2000).
39. J. A. E. Wasey and W. L. Barnes, "Efficiency of spontaneous emission from planar microcavities," J. Mod. Opt. **47**(4), 725–741 (2000).
40. D. Delbeke, R. Bockstaele, P. Bienstman, R. Baets, and H. Benisty, "High-efficiency semiconductor resonant-cavity light-emitting diodes: a review," IEEE J. Sel. Top. Quantum Electron. **8**(2), 189–206 (2002).
41. N. Danz, R. Waldhäusl, A. Bräuer, and R. Kowarschik, "Dipole lifetime in stratified media," J. Opt. Soc. Am. B **19**(3), 412–419 (2002).
42. H. Riel, S. Karg, T. Beierlein, and W. Rieß, "Tuning the emission characteristics of top-emitting organic light-emitting devices by means of a dielectric capping layer: An experimental and theoretical study," J. Appl. Phys. **94**(8), 5290 (2003).
43. D. Byrne, F. Natali, B. Damilano, A. Dussaigne, N. Grandjean, and J. Massies, "Blue Resonant Cavity Light Emitting Diodes with a High-Al-Content GaN/AlGaN Distributed Bragg Reflector," Jpn. J. Appl. Phys. **42**, L1509–L1511 (2003).
44. H.-J. Moon and D.-Y. Kang, "Strongly enhanced mode selection in a thin dielectric-coated layered microcavity laser," Opt. Lett. **32**(11), 1554–1556 (2007).
45. M. Kolle, B. Zheng, N. Gibbons, J. J. Baumberg, and U. Steiner, "Stretch-tuneable dielectric mirrors and optical microcavities," Opt. Express **18**(5), 4356–4364 (2010).
46. J. Sohn, Y. Kwon, Y. Lee, and C. Lee, "Light out-coupling efficiency enhancement in organic light-emitting diodes using a multilayer stacked electrode with sol-gel processed Ta_2O_5," Opt. Express **25**(22), 27886–27895 (2017).

Optics EXPRESS

47. C. Amra, C. Grezes-Besset, and L. Bruel, "Comparison of Surface and Bulk Scattering in Optical Multilayers," Appl. Opt. **32**(28), 5492–5503 (1993).
48. C. Amra, M. Zerrad, and M. Lequime, "Trapped light scattering within optical coatings: a multilayer roughness-coupling process," Opt. Express **29**(16), 25570–25592 (2021).